

PROCEEDINGS OF SPIE

[SPIDigitalLibrary.org/conference-proceedings-of-spie](https://spiedigitallibrary.org/conference-proceedings-of-spie)

Interlaminar stress analysis of shell structures with piezoelectric patch including thermal loading

Heung Soo Kim, Xu Zhou, Aditi Chattopadhyay

Heung Soo Kim, Xu Zhou, Aditi Chattopadhyay, "Interlaminar stress analysis of shell structures with piezoelectric patch including thermal loading," Proc. SPIE 4326, Smart Structures and Materials 2001: Modeling, Signal Processing, and Control in Smart Structures, (21 August 2001); doi: 10.1117/12.436489

SPIE.

Event: SPIE's 8th Annual International Symposium on Smart Structures and Materials, 2001, Newport Beach, CA, United States

Interlaminar Stress Analysis of Shell Structures with Piezoelectric Patch Including Thermal Loading

Heung Soo Kim, Xu Zhou and Aditi Chattopadhyay
Department of Mechanical and Aerospace Engineering
Arizona State University
Tempe, AZ 85287-6106

1. INTRODUCTION

The concept of smart structures, such as piezoelectric laminates, has received a great deal of attention recently as an alternative to conventional techniques. These advanced structures can be designed to actively react to disturbance forces in order to maintain structural integrity while maintaining, or even improving, the level of performance. Great potential can be found in advanced aerospace structural applications. However, the introduction of smart devices inevitably perturb the local values of the field variables and nucleate damage such as debonding and delamination at the interface of piezoelectric devices and the host structure due to stress concentration. The layerwise characteristics of the laminates make the determination of stress and strain distribution a challenging problem. Conventionally, classical lamination theory has been extended to smart laminated structures which ignores transverse shear effects¹⁻³. A higher order theory was proposed and applied by Chattopadhyay et al.^{4,5} in the analysis of laminated structures to address transverse shear effects without shear correction factors. The theory proved to be successful in global analysis for thick structures and smart structures. However, it fails to provide continuous distribution of transverse shear stresses. This implies that the theory is not sufficient in predicting local information regarding stress and strain distributions which is critical in the analysis of structural failure.

The multifield characteristics of piezoelectric structures make the analysis even more complex, particularly in the presence of thermal effects as dictated by specific missions. A typical environment is represented by a solar flux of 1350 W/m^2 as vehicles move from shadow to sunlight. Some research in the field of smart structural modeling in the presence of thermal effects has been reported⁶⁻¹⁰. However, one-way coupling that only considers the effect of a known field on another field is used in these works. The bi-way coupling between piezoelectric and mechanical fields was included in the hybrid plate theory developed by Mitchell and Reddy³. A coupled thermal-piezoelectric-mechanical (t-p-m) model was developed by Chattopadhyay et al.¹¹⁻¹³ to address the bi-way coupling issues associated with smart composites under thermal loads. Their work indicates that the effects of bi-way coupling on structural deformation increase with the thickness of piezoelectric device. However, an equivalent single layer approach is used, and therefore the localized interlaminar characteristics cannot be addressed accurately by this theory.

The present paper aims at the investigation of interlaminar stress distribution in laminated shell structures using coupled thermal-piezoelectric-mechanical model. The goal is to develop a theory that is capable of providing sufficient accuracy while guaranteeing computational efficiency compared to other layerwise theories. To maintain local accuracy of stress and strain distributions, the trial displacement field is assumed using zigzag functions and C_0 continuity through the entire laminate thickness accommodating zigzag in-plane warping and interlaminar transverse shear stress continuity. The continuity conditions of in-plane displacement and transverse shear stress fields as well as traction free boundary conditions are applied to reduce the number of primary structural variables. The temperature and electrical fields are assumed using higher order functions. These descriptions can satisfy surface boundary conditions of heat

flux and electrical potential. The mathematical model is implemented using finite element technique. The case of cylindrical bending and spherical composite shell structures with piezoelectric patches are investigated. The analysis of stress distributions under electrical and thermoelectrical loading is performed and numerical results are presented.

2. MODEL DEVELOPMENT

For the elastic system with piezoelectric materials as shown in Fig. 1, the linear constitutive relations can be expressed as follows.

$$\sigma_{ij} = c_{ijkl}\varepsilon_{kl} - e_{ijk}E_k - k_{ij}\theta; \quad D_i = e_{ijk}\varepsilon_{jk} + b_{ij}E_j + d_i\theta \quad (1)$$

where the quantities ε_{ij} and σ_{ij} denote the components of strain and stress tensors, respectively. The quantities E_i and D_i denote components of electric field and electric displacement, respectively and θ denotes the temperature rise from the initial temperature. In Eq. (1), five sets of material coefficients are used to address constitutive characteristics of mechanical, electrical and thermal fields as well as the coupling between these fields. The quantities c_{ijkl} , e_{ijk} and b_{ij} represent elastic constants, piezoelectric constants and dielectric permittivity, respectively. The quantities k_{ij} and d_i refer to thermal-mechanical and thermal-piezoelectric coupling constants, respectively.

2.1 Improved Shear Deformation Theory

Consider a shell element with N laminae described in orthogonal coordinates, α and β , along the shell mid-surface as shown in Fig. 1. The thickness coordinate, z , is measured from the mid-surface and R_α and R_β are the radii of curvature of the α and β -curves. The area of an infinitesimal rectangle dS and the volume of an infinitesimal parallelepiped dv are defined as follows.

$$dS = A_\alpha(1 + z/R_\alpha)A_\beta(1 + z/R_\beta) d\alpha d\beta; \quad dv = A_\alpha(1 + z/R_\alpha)A_\beta(1 + z/R_\beta) d\alpha d\beta dz \quad (2)$$

where A_α and A_β are the coefficients of the first fundamental form of the shell reference surface. In the present paper, the equilibrium of the shell element is described using layerwise functions as follows.

$$U_i^k(\alpha, \beta, z) = (1 + \frac{z}{R_i}) u_i(\alpha, \beta) + \phi_i(\alpha, \beta)f_i(z) + \theta_i^k(\alpha, \beta)g_i(z) + \psi_i^k(\alpha, \beta)h_i(z) \\ U_z^k(\alpha, \beta, z) = w(\alpha, \beta) \quad (3)$$

where the superscript k denotes the k -th layer of the laminate. The subscript i denotes the coordinate α or β . Laminate unknowns (u_i and ϕ_i) and layerwise unknowns (θ_i^k and ψ_i^k) are used to address in-plane deformation. Equation (3) states that the zigzag in-plane deformation can be described using a combination of laminate-wise first order shear deformation theory and layerwise higher order rotation. Note that Eq. (3) results in $4N + 5$ number of structural unknowns in the displacement field. The through-laminate-thickness functions, $f_i(z)$, $g_i(z)$ and $h_i(z)$, are used to address the characteristics of in-plane zigzag deformation, which have the following form.

$$f_i(z) = z; \quad g_i(z) = \sinh(z); \quad h_i(z) = \cosh(z) \quad (4)$$

where the function $f_i(z)$ denotes laminate rotation. The functions $g_i(z)$ and $h_i(z)$ render higher order odd and even distributions, respectively. The assumed displacement field can allow for discontinuous transverse shear strain at the laminate interfaces at the expense that the number of structural variables is dependent on the number of laminae. This implies that computation effort will increase greatly if multi-layered laminates

are used. Thus, the reduction in structural variables is necessary for the procedure to be cost effective in practical applications. The conditions of free transverse shear stress on the top and the bottom surfaces and the continuity conditions of transverse shear stress and in-plane displacement at interlaminar surfaces are used to reduce the number of structural variables. The details of the procedure are described in Ref. 14. Linear strain-displacement relationship¹⁵ is used in the present paper. Therefore, the displacement field can be expressed as follows.

$$U_1^k = \left(1 + \frac{z}{R_i}\right) u_\alpha + C_1^k(z)\phi_\alpha + D_1^k(z)\phi_\beta + E_1^k(z)w_{,\alpha} + F_1^k(z)w_{,\beta}$$

$$U_z^k = w \quad (5)$$

It must be noted that the structural unknowns describing the mechanical field, ranging from the first lamina to the N-th lamina, are reduced to only five variables, u_α , u_β , w , ϕ_α and ϕ_β . Therefore, the developed approach renders the number of structural variables independent of the number of laminae. All terms on the order of the thickness coordinate-to-radius are retained in the formulation, which makes the current approach applicable in the analysis of thick shell structures.

2.2 Higher Order Piezoelectric Field

The field of electric potential must satisfy the surface boundary condition of applied voltages accurately. Therefore, a cubic distribution of the potential field along the thickness of piezoelectric layers is assumed. The potential field (ϕ^j) for the j-th layer can be written as follows¹⁶.

$$\phi^j(\alpha, \beta, z) = \phi_0^j(\alpha, \beta) - (z - z_0^j)E_z^j(\alpha, \beta) + 4\left(\frac{z - z_0^j}{h^j}\right)^2 \left[(z - z_0^j)\left(\frac{\bar{\phi}^j}{h^j} + E_z^j(\alpha, \beta)\right) - \phi_0^j(\alpha, \beta) \right] \quad (6)$$

where ϕ_0^j is the potential of a point in the mid-plane of the k-th piezoelectric layer. The quantity E_z^j denotes the electric field of mid-plane and the term $-(z - z_0^j)E_z^j$ is used to address the linear potential distribution along the thickness. The last term in Eq. (6) represents the higher order modification addressing the nonuniform potential variation along the thickness while satisfying the equipotential surface boundary conditions prescribed at the electrodes. The quantity $\bar{\phi}^j$ denotes the potential difference between the top and the bottom electrodes covering the j-th piezoelectric transducer and z_0^j and h^j denote the mid-plane position and the thickness of the j-th piezoelectric layer, respectively.

2.3 Higher Order Temperature Field

The temperature field must satisfy surface boundary condition of heat flux accurately. To address nonuniform temperature distribution through the laminate thickness, temperature field is described using a cubic function of the thickness coordinate. By imposing surface boundary conditions of heat flux, the higher order temperature field can be written as follows¹²⁻¹³.

$$\theta(\alpha, \beta, z) = -\left(\frac{z^2}{2H} \frac{q_t - q_b}{\kappa_{33}} + \frac{2z^3}{3H^2} \frac{q_t + q_b}{\kappa_{33}}\right) + \theta_0(\alpha, \beta) + \left(z - \frac{4}{3H^2}z^3\right)\theta_1(\alpha, \beta) \quad (7)$$

where the quantities q_t and q_b indicate the heat flux applied on top and the bottom surfaces, respectively. The quantity κ_{33} denotes thermal conductivity through the thickness and H represents the total thickness of the laminate. The higher order temperature field defines a nonuniform cubic distribution through the thickness of the structure. It is important to note that although a linear temperature field can address the in-

plane temperature distribution, it cannot satisfy the surface thermal boundary conditions. Thus, temperature variations through the thickness, which produce the most important bending deformation, cannot be modeled accurately using linear temperature field.

3. FINITE ELEMENT IMPLEMENTATION

The finite element implementation of a shell element with piezoelectric layers using thermal-piezoelectric-mechanical coupling model is considered. The displacement and temperature unknowns of the element are denoted. \mathbf{u}_u^e and \mathbf{u}_θ^e , respectively. The electrical unknowns of the j -th piezoelectric layer are denoted $\mathbf{u}_\phi^{e,j}$. The displacement field in the mid-plane of the element ($\mathbf{u}_{u0}(\alpha, \beta)$), the electrical field in the mid-plane of the j -th piezoelectric layer ($\mathbf{u}_{\phi0}^j(\alpha, \beta)$) and the temperature field in the mid-plane of the element ($\mathbf{u}_{\theta0}(\alpha, \beta)$) can be expressed using appropriate interpolation functions as follows.

$$\mathbf{u}_{u0}(\alpha, \beta) = [\mathbf{u}_\alpha, \mathbf{u}_\beta, w, \phi_\alpha, \phi_\beta]^T = \mathbf{N}_u(\alpha, \beta) \mathbf{u}_u^e; \quad \mathbf{u}_{\phi0}^j(\alpha, \beta) = [\phi_0^j, E_z^j]^T = \mathbf{N}_\phi(\alpha, \beta) \mathbf{u}_\phi^{e,j}$$

$$\mathbf{u}_{\theta0}(\alpha, \beta) = [\theta_0, \theta_1]^T = \mathbf{N}_\theta(\alpha, \beta) \mathbf{u}_\theta^e \quad (8)$$

where $\mathbf{N}_u(\alpha, \beta)$, $\mathbf{N}_\phi(\alpha, \beta)$ and $\mathbf{N}_\theta(\alpha, \beta)$ are the interpolation functions for displacement, potential field and temperature field, respectively.

Based on the field assumption described in the present paper, the element displacement field $\mathbf{u}(\alpha, \beta, z)$, the strain $\boldsymbol{\varepsilon}(\alpha, \beta, z)$, the potential field $\phi^j(\alpha, \beta, z)$, the electric field $\mathbf{E}^j(\alpha, \beta, z)$, the temperature field $\theta(\alpha, \beta, z)$ and the gradient of temperature field $\theta_{,i}(\alpha, \beta, z)$ can be written as follows.

$$\mathbf{u}(\alpha, \beta, z) = \mathbf{L}_u \mathbf{u}_{u0}(\alpha, \beta); \quad \boldsymbol{\varepsilon}(\alpha, \beta, z) = \mathbf{L}_\varepsilon \mathbf{u}_{u0}(\alpha, \beta)$$

$$\phi^j(\alpha, \beta, z) = F_\phi(z - z_0^j) + \mathbf{L}_\phi^j \mathbf{u}_{\phi0}^j(\alpha, \beta); \quad -\mathbf{E}^j(\alpha, \beta, z) = \mathbf{F}_E(z - z_0^j) + \mathbf{L}_E^j \mathbf{u}_{\phi0}^j(\alpha, \beta) \quad (9)$$

$$\theta(\alpha, \beta, z) = F_\theta(z) + \mathbf{L}_\theta \mathbf{u}_{\theta0}(\alpha, \beta); \quad \theta_{,i}(\alpha, \beta, z) = \mathbf{F}_p(z) + \mathbf{L}_p \mathbf{u}_{\theta0}(\alpha, \beta)$$

where the higher order operators, \mathbf{L}_u and \mathbf{L}_ε , are defined as follows.

$$\mathbf{L}_u = \begin{bmatrix} 1 + z/R_\alpha & 0 & E_\alpha^k(z) \partial/\partial\alpha + F_\alpha^k(z) \partial/\partial\beta & C_\alpha^k(z) & D_\alpha^k(z) \\ 0 & 1 + z/R_\beta & E_\beta^k(z) \partial/\partial\alpha + F_\beta^k(z) \partial/\partial\beta & C_\beta^k(z) & D_\beta^k(z) \\ 0 & 0 & 1 & 0 & 0 \end{bmatrix} \quad (10)$$

$$\mathbf{L}_\varepsilon = \begin{bmatrix} A_\alpha^{-1} \frac{\partial}{\partial\alpha} & 0 & Z_\alpha + E_\alpha^k P_\alpha^{-1} \frac{\partial^2}{\partial\alpha^2} + F_\alpha^k P_\alpha^{-1} \frac{\partial^2}{\partial\alpha\partial\beta} & C_\alpha^k P_\alpha^{-1} \frac{\partial}{\partial\alpha} & D_\alpha^k P_\alpha^{-1} \frac{\partial}{\partial\alpha} \\ 0 & A_\beta^{-1} \frac{\partial}{\partial\beta} & Z_\beta + E_\beta^k P_\beta^{-1} \frac{\partial^2}{\partial\alpha\partial\beta} + F_\beta^k P_\beta^{-1} \frac{\partial^2}{\partial\beta^2} & C_\beta^k P_\beta^{-1} \frac{\partial}{\partial\beta} & D_\beta^k P_\beta^{-1} \frac{\partial}{\partial\beta} \\ 0 & 0 & \left(E_{\beta,z}^k - E_\beta^k Z_\beta \right) \frac{\partial}{\partial\alpha} + \left(F_{\beta,z}^k - F_\beta^k Z_\beta + P_\beta^{-1} \right) \frac{\partial}{\partial\beta} & C_{\beta,z}^k - C_\beta^k Z_\beta & D_{\beta,z}^k - D_\beta^k Z_\beta \\ 0 & 0 & \left(E_{\alpha,z}^k - E_\alpha^k Z_\alpha + P_\alpha^{-1} \right) \frac{\partial}{\partial\alpha} + \left(F_{\alpha,z}^k - F_\alpha^k Z_\alpha \right) \frac{\partial}{\partial\beta} & C_{\alpha,z}^k - C_\alpha^k Z_\alpha & D_{\alpha,z}^k - D_\alpha^k Z_\alpha \\ \frac{\partial/\partial\beta}{Z_\alpha R_\alpha P_\beta} & \frac{\partial/\partial\alpha}{Z_\beta R_\beta P_\alpha} & \frac{E_\beta^k}{P_\alpha} \frac{\partial^2}{\partial\alpha^2} + \left(\frac{F_\beta^k}{P_\alpha} + \frac{E_\alpha^k}{P_\beta} \right) \frac{\partial^2}{\partial\alpha\partial\beta} + \frac{F_\alpha^k}{P_\beta} \frac{\partial^2}{\partial\beta^2} & \frac{C_\beta^k}{P_\alpha} \frac{\partial}{\partial\alpha} + \frac{C_\alpha^k}{P_\beta} \frac{\partial}{\partial\beta} & \frac{D_\beta^k}{P_\alpha} \frac{\partial}{\partial\alpha} + \frac{D_\alpha^k}{P_\beta} \frac{\partial}{\partial\beta} \end{bmatrix}$$

with

$$Z_\alpha = (z + R_\alpha)^{-1}; \quad Z_\beta = (z + R_\beta)^{-1}; \quad P_\alpha = A_\alpha \left(1 + \frac{z}{R_\alpha} \right); \quad P_\beta = A_\beta \left(1 + \frac{z}{R_\beta} \right) \quad (11)$$

The higher order operators and functions related with electrical field, \mathbf{L}_ϕ^j , \mathbf{L}_E^j , F_ϕ and \mathbf{F}_E , are defined as follows.

$$\mathbf{L}_\phi^j = \left[1 - 4(z - z_0^j)^2 / (h^j)^2, -(z - z_0^j) + 4(z - z_0^j)^3 / (h^j)^2 \right]$$

$$\mathbf{L}_E^j = \begin{bmatrix} \left[1 - 4(z - z_0^j)^2 / (h^j)^2 \right] \partial / \partial \alpha & \left[4(z - z_0^j)^3 / (h^j)^2 - (z - z_0^j) \right] \partial / \partial \alpha \\ \left[1 - 4(z - z_0^j)^2 / (h^j)^2 \right] \partial / \partial \beta & \left[4(z - z_0^j)^3 / (h^j)^2 - (z - z_0^j) \right] \partial / \partial \beta \\ -8(z - z_0^j) / (h^j)^2 & 12(z - z_0^j)^2 / (h^j)^2 - 1 \end{bmatrix} \quad (12)$$

$$F_\phi(z - z_0^j) = 4\bar{\phi}^j (z - z_0^j)^3 / (h^j)^3; \quad \mathbf{F}_E(z - z_0^j) = \begin{bmatrix} 0 & 0 & 12\bar{\phi}^j (z - z_0^j)^2 / (h^j)^3 \end{bmatrix}^T$$

The higher order operators and functions related with thermal field, \mathbf{L}_θ , \mathbf{L}_p , F_θ and \mathbf{F}_p , are defined as follows.

$$\mathbf{L}_\theta = \begin{bmatrix} 1 & z - 4z^3 / 3H^2 \end{bmatrix}; \quad \mathbf{L}_p = \begin{bmatrix} \partial / \partial \alpha & \left(z - 4z^3 / 3H^2 \right) \partial / \partial \alpha \\ \partial / \partial \beta & \left(z - 4z^3 / 3H^2 \right) \partial / \partial \beta \\ 0 & \left(1 - 4z^2 / H^2 \right) \end{bmatrix} \quad (13)$$

$$F_\theta(z) = - \left(\frac{z^2}{2H} \frac{q_t - q_b}{\kappa_{33}} + \frac{2z^3}{3H^2} \frac{q_t + q_b}{\kappa_{33}} \right); \quad \mathbf{F}_p(z) = \begin{bmatrix} 0 & 0 & dF_\theta(z) / dz \end{bmatrix}^T$$

The linear thermo-electro-mechanical multiple field problem for a domain V without free body charge, based on displacement, electric potential and temperature as independent state variables, can be described using variational principle along with several constraints as follows.

$$\delta\pi(\mathbf{u}_i, \phi, \theta) = \int_V (\sigma_{ij} \delta\epsilon_{ij} - D_i \delta\phi_{,i} + \kappa_{ij} \theta_{,i} \delta\theta_{,j}) dV - \int_{\Gamma_\sigma} \bar{t}_i \delta u_i d\Gamma + \int_{\Gamma_D} \bar{q}_e \delta\phi d\Gamma + \int_{\Gamma_q} \bar{q}_s \delta\theta d\Gamma = 0 \quad (14)$$

Equation (14) addresses temperature, piezoelectric and mechanical fields simultaneously and represents the governing equations of the coupled thermo-piezoelectric-mechanical theory. The quantities \bar{t}_i , \bar{q}_e and \bar{q}_s denote the prescribed traction on the stress boundary Γ_σ , surface charge on the charge boundary Γ_D and surface heat flux on the flux boundary Γ_q , respectively.

Substituting Eq. (9) into Eq. (14), the following finite element governing equations of the thermo-piezoelectric-mechanical coupled theory are obtained.

$$\begin{bmatrix} \mathbf{K}_{uu} & \mathbf{K}_{u\phi} & \mathbf{K}_{u\theta} \\ \mathbf{K}_{\phi u} & \mathbf{K}_{\phi\phi} & \mathbf{K}_{\phi\theta} \\ 0 & 0 & \mathbf{K}_{\theta\theta} \end{bmatrix} \begin{Bmatrix} \mathbf{u}_u^e \\ \mathbf{u}_\phi^e \\ \mathbf{u}_\theta^e \end{Bmatrix} = \begin{Bmatrix} \mathbf{F}_u \\ \mathbf{F}_\phi \\ \mathbf{F}_\theta \end{Bmatrix} \quad (15)$$

where the matrices $\mathbf{K}_{u\phi}$ and $\mathbf{K}_{\phi u}$ are stiffness matrices due to piezoelectric-mechanical coupling effect, and $\mathbf{K}_{u\theta}$ and $\mathbf{K}_{\phi\theta}$ are stiffness matrices due to thermal-mechanical and thermal-electrical coupling, respectively. The matrices \mathbf{K}_{uu} , $\mathbf{K}_{\phi\phi}$ and $\mathbf{K}_{\theta\theta}$ are stiffness matrices due to mechanical, electrical and thermal fields, respectively. The vectors \mathbf{F}_u , \mathbf{F}_ϕ and \mathbf{F}_θ are force vectors due to mechanical, electrical and thermal fields, respectively. The stiffness matrices and force vectors are defined as follows.

$$\mathbf{K}_{uu} = \int_V \mathbf{B}_\epsilon^T \mathbf{Q} \mathbf{B}_\epsilon dV; \quad \mathbf{K}_{u\phi} = \int_V \mathbf{B}_\epsilon^T \mathbf{P} \mathbf{B}_\phi dV; \quad \mathbf{K}_{u\theta} = - \int_V \mathbf{B}_\epsilon^T \mathbf{k} \mathbf{B}_\theta dV; \quad \mathbf{K}_{\phi u} = - \mathbf{K}_{u\phi}^T$$

$$\begin{aligned}
\mathbf{K}_{\phi\phi} &= \int_V \mathbf{B}_E^T \mathbf{B} \mathbf{B}_E dV; & \mathbf{K}_{\phi\theta} &= -\int_V \mathbf{B}_E^T d\mathbf{B}_\theta dV; & \mathbf{K}_{\theta\theta} &= \int_V \mathbf{B}_p^T \kappa \mathbf{B}_p dV \\
\mathbf{F}_u &= \int_S \mathbf{B}_u^T t dS - \int_V \mathbf{B}_\varepsilon^T \mathbf{k} \left(\frac{z^2}{2H} \frac{q_t - q_b}{\kappa_{33}} + \frac{2z^3}{3H^2} \frac{q_t + q_b}{\kappa_{33}} \right) dV - \int_V \mathbf{B}_\varepsilon^T \mathbf{P} \mathbf{F}_b (z - z_0^j) dV \\
\mathbf{F}_\phi &= -\int_S \mathbf{B}_\phi^T q_e dS - \int_V \mathbf{B}_E^T \mathbf{B} \mathbf{F}_b (z - z_0^j) dV - \int_V \mathbf{B}_\phi^T \mathbf{d} \left(\frac{z^2}{2H} \frac{q_t - q_b}{\kappa_{33}} + \frac{2z^3}{3H^2} \frac{q_t + q_b}{\kappa_{33}} \right) dV \\
\mathbf{F}_\theta &= -\int_S \mathbf{B}_\theta^T q_t dS - \int_V \mathbf{B}_p^T \kappa \mathbf{F}_p (z) dV
\end{aligned} \tag{16}$$

with the definition of the operators as follows.

$$\begin{aligned}
\mathbf{B}_u &= \mathbf{L}_u \mathbf{N}_u(\alpha, \beta); & \mathbf{B}_\varepsilon &= \mathbf{L}_\varepsilon \mathbf{N}_\varepsilon(\alpha, \beta); & \mathbf{B}_\phi^j &= \mathbf{L}_\phi^j \mathbf{N}_\phi(\alpha, \beta) \\
\mathbf{B}_E^j &= \mathbf{L}_E^j \mathbf{N}_E(\alpha, \beta); & \mathbf{B}_\theta &= \mathbf{L}_\theta \mathbf{N}_\theta(\alpha, \beta); & \mathbf{B}_p &= \mathbf{L}_p \mathbf{N}_p(\alpha, \beta)
\end{aligned} \tag{17}$$

4. RESULTS AND DISCUSSIONS

First, the effectiveness and accuracy of the proposed displacement description is evaluated by comparison with other theories. The bending of a three-layer symmetric cylindrical laminated shell with layers of equal thickness and fibers parallel to the α and β directions in the outer and central layers, respectively, is investigated. The cylinder is simply supported and is infinite in α direction. The radius of curvature $R_\beta = R = 10$ and the span angle $\varphi = \pi/3$. The material properties are such that $E_L = 172 \text{ GPa}$, $E_T = 6.9 \text{ GPa}$, $G_{LT} = 3.4 \text{ GPa}$, $G_{TT} = 1.4 \text{ GPa}$ and $\nu_{LT} = \nu_{TT} = 0.25$. The subscripts L and T denote the fiber direction and transverse direction, respectively. A transverse normal loading, $q_0 \sin(3\beta)$, is applied on the top surface. The quantity S is defined as the ratio of the radius of curvature to structural thickness, that is, $S = R/H$. The results from the present theory are compared with those obtained using the CLT and the elasticity solution by Ren¹⁷. Table 1 presents comparison of central transverse deflection (maximum deflection), in-plane normal stress at the top and the bottom surfaces and edge transverse shear stress at the mid-plane of the top layer for values of radius-to-thickness ratio (S) ranging from 2 to 100. The results are nondimensionalized as follows.

$$\bar{W}(z) = \frac{10 E_T U_z(\varphi/2, z)}{q_0 H S^4}; \quad \bar{\tau}_{\beta z}(z) = \frac{\tau_{\beta z}(0, z)}{q_0 S}; \quad \bar{\sigma}_\beta(z) = \frac{\sigma_\beta(\varphi/2, z)}{q_0 S^2} \tag{18}$$

As seen from Table 1, at values of $R/H \geq 50$ (thin constructions), the differences between deflection and normal stress prediction obtained from the CLT, the elasticity solution and the present theory are negligible. However, at values of $R/H \leq 50$ (thick constructions), the results obtained from the CLT deviate from those obtained using the elasticity solution and the present theory. This is due to the fact that CLT ignores transverse shear effects. At $R/h = 4$, the deviations in deflection between present model and elasticity solution is 7 percent whereas the deviation is 83 percent in case of CLT. In in-plane normal stress predictions, at the bottom and the top surfaces, the present model deviates by only 1.7 and 0.5 percent respectively from elasticity solution. The corresponding deviations are 54 and 46 percent, respectively in case of CLT. The present theory also provides good prediction of transverse shear stress. The deviation of shear stress at the mid surface from the exact solution using the present model is about 2.1 percent. Therefore, the present model shows excellent correlation with the elasticity solution for all radius-to-thickness ratios.

Table 1 Nondimensionalized Deflection and Stresses in [0/90/0] Cylindrical Shell under Sinusoidal Loading.

	R/h	$\bar{W}(0)$	$\bar{\sigma}_\beta(\mp H/2)$	$\bar{\tau}_{\beta z}(0)$		R/h	$\bar{W}(0)$	$\bar{\sigma}_\beta(\mp H/2)$	$\bar{\tau}_{\beta z}(0)$
CLT		0.0799	-0.870 0.686	----	CLT		0.0776	-0.792 0.774	----
Elasticity	2	1.436	-3.467 2.463	0.394	Elasticity	50	0.0808	-0.798 0.782	0.526
Present		1.535	-4.025 2.081	0.383	Present		0.0814	-0.794 0.786	0.533
CLT		0.0781	-0.824 0.732	----	CLT		0.0776	-0.779 0.776	----
Elasticity	4	0.457	-1.772 1.367	0.476	Elasticity	100	0.0787	-0.786 0.781	0.523
Present		0.489	-1.802 1.374	0.486	Present		0.0788	-0.784 0.780	0.531
CLT		0.0777	-0.796 0.759	----					
Elasticity	10	0.144	-0.995 0.897	0.525					
Present		0.150	-0.986 0.920	0.532					

Table 2 Material Properties of PZT and Graphite/Epoxy Composite.

	PZT	Graphite/Epoxy	PZT	Graphite/Epoxy
Elastic Moduli (GPa):			Piezoelectric Charge Constant (pm/V):	
E_{11}	63	144.23	$e_{31}=e_{32}$	150
E_{22}	63	9.65	Electric Permittivity (nf/m):	
E_{33}	63	9.65	b_{33}	15.0
Shear Moduli (GPa):			b_{33}	15.0
G_{23}	24.6	3.45	Pyroelectric Constant ($\mu\text{C}/\text{m}^2\text{-}^\circ\text{C}$)	
G_{13}	24.6	4.14	d_3	20
G_{12}	24.6	4.14	Thermal Conductivity (W/m- $^\circ\text{C}$):	
Poisson's Ratio:			κ_{11}	2.1
ν	0.28	0.3	κ_{33}	2.1
Coefficients of Thermal Expansion ($\mu\text{m}/\text{m-}^\circ\text{C}$):				
α_{11}	0.9	1.1		
α_{33}	0.9	25.2		

Next, the numerical analysis of a spherical fiber-reinforced laminated composite shell (Graphite/Epoxy) with surface-bonded piezoelectric transducers under various loading conditions is considered. Four piezoelectric patches are used to produce desired actuation capability for shape control as shown in Fig. 1. Each patch comprises actuators bonded on the top and the bottom surfaces of the structure. The shell structure is fixed on all four sides. The material constants for the composite and the piezoelectric materials are listed in Table 2. The shell dimensions are such that the radii of curvature $R_\alpha = R_\beta = 0.64\text{m}$, arc length $a = 0.64\text{m}$, arc width $b = 0.64\text{m}$ and the thickness of the primary composite $h = a/10$. The configurations of piezoelectric actuators are such that the thickness is $h/6$, the width and length are each $a/5$. The actuators are located at the center of each quarter section of the structure (as shown in Fig. 1).

A two-layer antisymmetric laminate with stacking sequence of [90/0] and equal lamina thickness is used to investigate the effects of thermal-piezoelectric-mechanical coupling. Only piezoelectric actuation is considered. Both the top and the bottom actuators are subjected to a voltage load of same magnitude but opposite directions, making out-of-plane deformation dominant. Note that in this case, the t-p-m model for actuators represents bi-way mechanical-piezoelectric coupling (piezoelectric and converse piezoelectric effects) while conventional induced strain model represents only one-way mechanical-piezoelectric

coupling (converse piezoelectric effect). Figure 2 presents the distributions of in-plane normal stresses, $\sigma_{\alpha\alpha}$ and $\sigma_{\beta\beta}$, through laminate thickness under electrical loading with a piezoelectric actuation of 100 V. The results are presented for the point A located in the structural element with piezoelectric actuator (as shown in Fig. 1). It can be observed that the distributions of in-plane normal stresses are discontinuous at the layer interfaces due to material dissimilarity. For both $\sigma_{\alpha\alpha}$ and $\sigma_{\beta\beta}$, the variation of the stresses through actuator thickness is not significant. However, the maximum stress occurs at the interfaces of the piezoelectric actuators and the primary structure which makes structural integrity a critical issue in these regions. The maximum values of $\sigma_{\alpha\alpha}$ and $\sigma_{\beta\beta}$ occur at the interfaces of the top and bottom actuators, respectively. The stress distribution in the primary structure is induced by the extension of top actuator and the compression of the bottom actuator. Figure 3 presents the distributions of transverse shear stress through laminate thickness under the same electrical loading. It can be observed that the transverse shear stresses vanish at the top and the bottom surfaces and are continuous at each interlaminar surface. The distributions show a significant gradient in actuator layers. Although the maximum shear stress occurs at the mid-plane of the structure, the interlaminar shear stresses at the interface of the actuators and the primary structure are up to 90 percent of the maximum value, which makes mode II and III failure (both laminate delamination and actuator debonding) critical.

Next, numerical analysis with only thermal excitations is performed to investigate thermal coupling effects. The same structural configuration is used. A uniform heat flux is applied on the top surface of the structure and it is insulated at the bottom. All four sides are maintained at room temperature (20 °C). Thermal steady state is achieved when there is an equilibrium between the inflow of surface heat flux and heat outflow through the four sides of the structure. Note that although there is no external voltage, all coupling effects between thermal, piezoelectric and mechanical fields are still present in the t-p-m model. Numerical results under a heat flux $q_t = 3000\text{W/m}^2$ are presented in Figs. 4-6. Figures 4 and 5 present the distribution of in-plane normal stresses and transverse shear stresses, respectively. For normal stresses, the stress distribution shows discontinuity due to the mismatch of thermal material properties. The maximum stress occurs at the interfaces of the actuator and the primary structures, up to 19 MPa for $\sigma_{\alpha\alpha}$ and 25 MPa for $\sigma_{\beta\beta}$. For transverse shear, the values of these stresses at the interlaminar surfaces between the actuators and the primary structure are close to the maximum. Figure 6 shows the temperature rise of the mid surface of the structure. The temperature rise in the structure is a result of the heat flow from the top surface to the side boundaries where heat finally dissipates. The temperature rise is maximum at the center of the structure and has the smallest values near the structural side boundaries. The temperature distribution is also symmetric since the geometry of the shell, the thermal boundary conditions and the external loading are all symmetric.

A three-layer symmetric laminated shell with stacking sequence of [0/90/0] and same configuration as above is considered next. Figures 7 and 8 present the distribution of in-plane normal stresses and transverse shear stresses under the same electrical voltage (100V) applied to the actuators. For in-plane normal stress, the same trend can be observed as in the case of antisymmetric [90/0] laminate. The maximum values of stress occur at the interfaces of the actuators and primary structure. However, for transverse shear stresses ($\sigma_{\alpha z}$ and $\sigma_{\beta z}$) significant deviations are observed from the case of [90/0] laminate due to the fact that fiber orientation makes the current configuration 0° dominant while the [90/0] laminate is quasi-isotropic. Control effects using various electrical loading are illustrated in Figs. 9 and 10. Figure 9 presents the structural deflection under symmetric piezoelectric loading, which implies that the same voltages (both magnitude and direction) are applied to each actuator. Figure 10 presents the deflection under antisymmetric piezoelectric loading. This implies that the diagonal actuators are subject to same electrical

voltages but the actuators adjacent to each other are subject to voltages with same magnitude but opposite directions. As seen from Figs. 9 and 10, multiple control objectives can be achieved for the same structural configuration using different loading.

Finally, numerical analysis on the [0/90/0] laminate subject to the same thermal excitations ($q_t = 3000\text{W}/\text{m}^2$) and same geometric boundary conditions as before is performed. Figures 11 and 12 present the distribution of in-plane normal stresses and transverse shear stresses, respectively. For normal stress, the stress distribution shows the same trend as in the case of [90/0] laminate. The maximum values of stress which occur at the interfaces of the actuator and the primary structure marginally deviate from those of the [90/0] case due to the same loading used. However, large deviations in transverse shear stresses ($\sigma_{\alpha z}$ and $\sigma_{\beta z}$) are observed from the [90/0] case, resulting from 0° dominant fiber orientation in the present case.

5. CONCLUDING REMARKS

An improved coupled theory is developed to address the effects of piezoelectric actuation under various kinds of loading conditions. A new layerwise shear deformation theory, developed to accommodate the complexity of in-plane zigzag warping and continuity of transverse shear stress distribution, is used in conjunction with the completely coupled thermal-piezoelectric-mechanical theory. The developed theory provides a framework for accurate and efficient analysis of stress distribution in composite shell structures integrated with piezoelectric materials. Numerical analysis is performed to investigate laminated composite shells with multiple surface bonded actuators. Piezoelectric loading and thermal loading are considered. The induced deflections and stress distributions are presented. The following important observations are made from this study.

1. The improved shear deformation theory correlates well with elasticity solutions. The use of the higher order electric and temperature fields in the thermal-piezoelectric-mechanical model make the developed approach applicable to a large class of smart structures.
2. In the analysis of structural bending due to piezoelectric actuation, for both symmetric and antisymmetric laminations, the maximum in-plane normal stresses and 90 percent of the maximum transverse shear stresses occur at the interface of the actuators and the primary structure. Thus structural integrity becomes a critical issue.
3. In the analysis of structural bending due to thermal actuation, for both symmetric and antisymmetric laminations, the results of stress analysis show that significant thermal mismatch occur at the interface between the actuator and the primary structure. This results in stress concentrations at those interfaces.

ACKNOWLEDGEMENTS

The research is supported by NASA Langley Research Center, grant number NAG-1-2283, technical monitor Dr. D. Ambur.

REFERENCES

1. Crawley, E. F., and de Luis, J., "Use of Piezoelectric Actuators as Elements of Intelligent Structures," *AIAA Journal*, Vol. 25, No. 10, 1987, pp. 1373-1385.
2. Lee, C. K., "Theory of Laminated Piezoelectric Plates for the Design of Distributed Sensors/Actuators. Part I: Governing Equations and Reciprocal Relationships," *Journal of the Acoustical Society of America*, Vol. 87, Vol. 3, 1990, pp. 1144-1158.

3. Mitchell, J. A., and Reddy, J. N., "A Refined Hybrid Plate Theory for Composite Laminates with Piezoelectric Laminae," *International Journal of Solids Structure*, Vol. 32, No. 16, 1995, pp. 2345-2367.
4. Chattopadhyay, A., and Gu, H., "New Higher Order Plate Theory in Modeling Delamination Buckling of Composite Laminates," *AIAA Journal*, Vol. 32, No. 8, 1994, pp. 1709-1716.
5. Chattopadhyay, A., and Seeley, C. E., "A Higher Order Theory for Modeling Composite Laminates with Induced Strain Actuators," *Composite Part B Engineering*, Vol. 28B, No. 8, 1997, pp. 243-252.
6. Mindlin, R. D., "Equations of High Frequency Vibrations of Thermopiezoelectric Crystal Plates," *International Journal of Solids Structure*, Vol. 10, 1974, pp. 625-632.
7. Mukherjee, N., and Sinha, P. K., "A Finite Element Analysis of Thermostructural Behavior of Composite Plates," *Journal of Reinforced Plastics and Composites*, Vol. 12, No. 11, 1993, pp. 1026-1042.
8. Tauchert, T. R., "Piezothermoelastic Behavior of a Laminated Plate," *Journal of Thermal Stresses*, Vol. 15, No. 1, 1992, pp. 25-37.
9. Lee, H., and Saravanos, D. A., "The Effect of Temperature Induced Material Property Variations on Piezoelectric Composite Plates," *Proceedings of the AIAA/ASME/ASCE/AHS/ASC 37th Structures, Structural Dynamics and Materials Conference*, AIAA, Salt Lake City, UT, 1996, pp. 1781-1788.
10. Lee, H., and Saravanos, D. A., "Active Compensation of Thermally Induced Bending and Twisting in Piezoceramic Composite Plates," *Proceedings of the AIAA/ASME/ASCE/AHS/ASC 38th Structures, Structural Dynamics and Materials Conference*, AIAA, Kissimmee, FL, 1997, pp. 120-130.
11. Chattopadhyay, A., Li, J., and Gu, H., "Coupled Thermo-Piezoelectric-Mechanical Model For Smart Composite Laminates," *AIAA Journal*, Vol. 37, No. 12, 1999, pp. 1633-1638.
12. Chattopadhyay, A., Gu, H., and Li, J., "A Coupled Thermo-Piezoelectric-Mechanical Theory For Smart Composites Under Thermal Load," *Proceedings of Ninth International Conference On Adaptive Structures & Technologies*, Cambridge, MA, 1998.
13. Zhou, X., Chattopadhyay, A., and Gu, H., "Dynamic Response of Smart Composites Using a Coupled Thermo-Piezoelectric-Mechanical Model," *AIAA Journal*, Vol. 38, No. 10, 2000, pp. 1939-1948.
14. Zhou, X. and Chattopadhyay, A., "An Improved Higher Order Theory for Laminated Shells Addressing Transverse Stress Continuity," *Proceedings of the AIAA/ASME/ASCE/AHS/ASC 41th Structures, Structural Dynamics and Materials Conference*, AIAA 2001-1338, Seattle, WA, 2001.
15. Calcote, L. R., "The Analysis of Laminated Composite Structures," Van Nostrand Reinhold Company, 1969.
16. Zhou, X., Chattopadhyay, A., and Thornburgh, R., "Analysis of Piezoelectric Smart Composites Using a Coupled Piezoelectric-Mechanical Model," *Journal of Intelligent Material Systems and Structures*, Vol. 11, 2000, pp. 169-179.
17. Ren, J. G., "Exact Solution for Laminated Cylindrical Shells in Cylindrical Bending," *Composites Science and Technology*, Vol. 29, 1987, pp. 169-187.

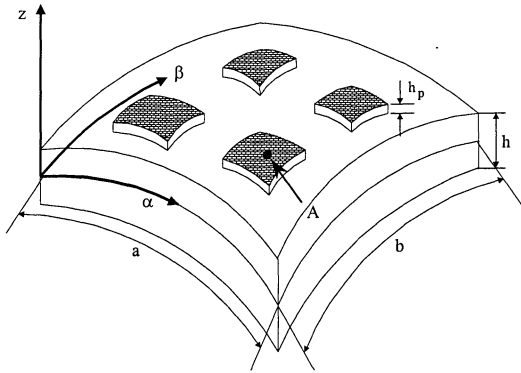


Fig. 1 Illustration of lamination.

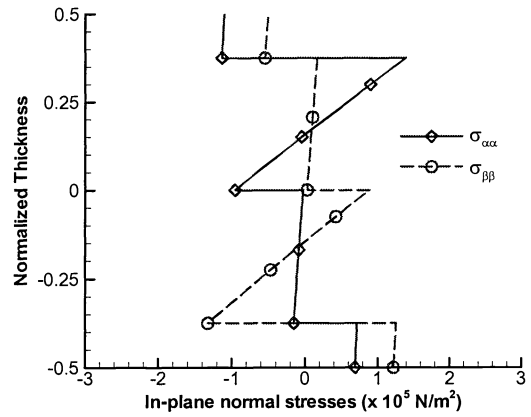


Fig. 2 Electrically induced in-plane normal stress distribution, [90/0].

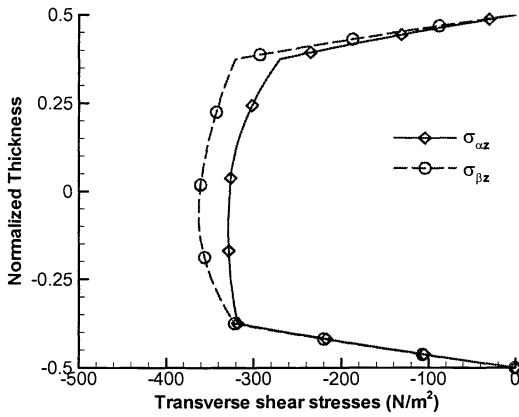


Fig. 3 Electrically induced transverse shear stress distribution, [90/0].

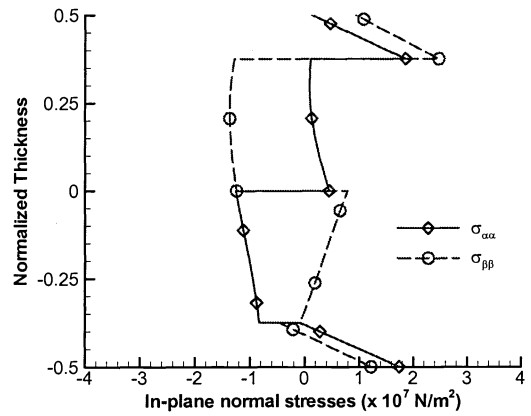


Fig. 4 Thermally induced in-plane normal stress distribution, [90/0].

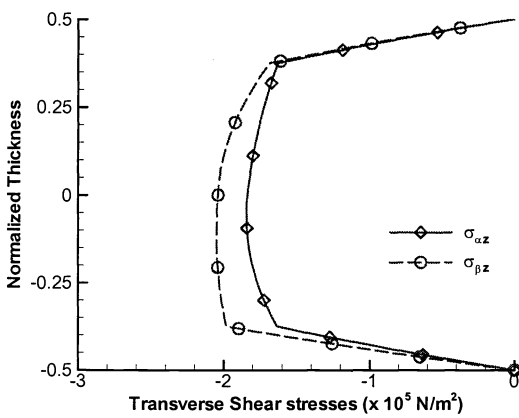


Fig. 5 Thermally induced transverse shear stress distribution, [90/0].

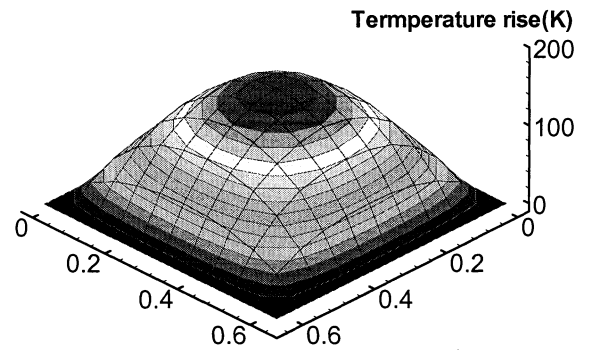


Fig. 6 Temperature rise at the mid surface, [90/0].

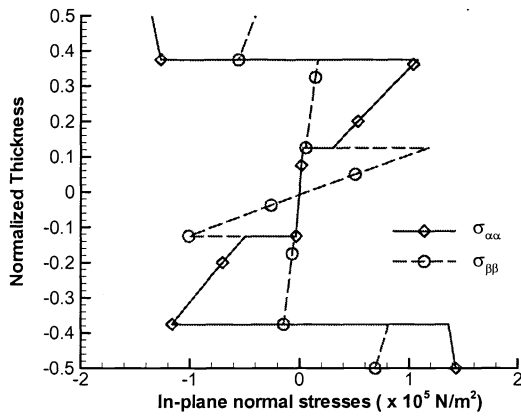


Fig. 7 Electrically induced in-plane normal stress distribution, [0/90/0].

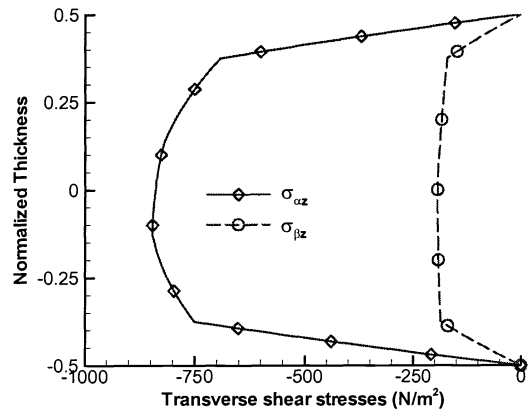


Fig. 8 Electrically induced transverse shear stress distribution, [0/90/0].

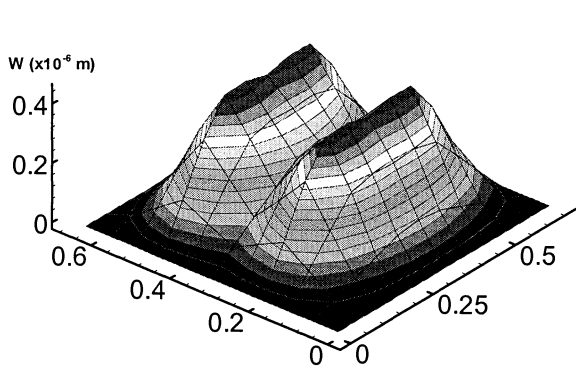


Fig. 9 Deflection under symmetric electric loading, [0/90/0].

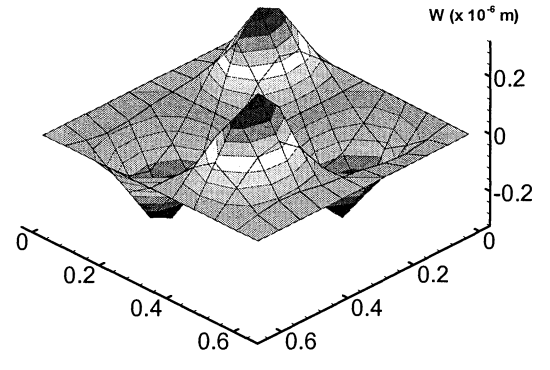


Fig. 10 Deflection under antisymmetric electric loading, [0/90/0].

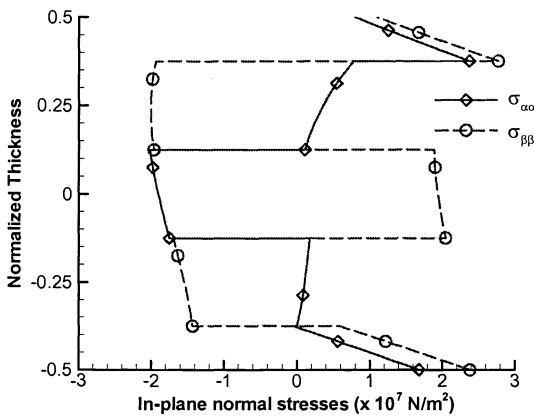


Fig. 11 Thermally induced in-plane normal stress distribution, [0/90/0].

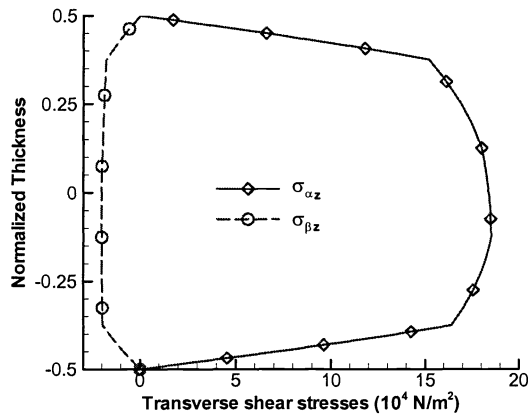


Fig. 12 Thermally induced transverse shear stress distribution, [0/90/0].